Journal of Materials Processing Tech. 263 (2019) 207–222

Contents lists available at ScienceDirect

Journal of Materials Processing Tech.

journal homepage: www.elsevier.com/locate/jmatprotec

Small strain finite element modelling of friction stir spot welding of Al and Mg alloys

P. Jedrasiak[a,b], H.R. Shercliff[a,*]

[a] Department of Engineering, University of Cambridge, Trumpington St, CB2 1PZ, UK
[b] TWI, Granta Park, Cambridge, CB21 6AL, UK

ARTICLE INFO

Keywords:
Friction stir spot welding
Aluminium alloys
Magnesium alloys
Process modelling
Finite element analysis

ABSTRACT

A finite element model was developed to predict the spatial and temporal variation of heat generation and temperature in FSSW of aluminium and magnesium alloys. Heating by friction and bulk plasticity is computed at intervals using small-strain elastic-plastic analysis for a small fraction of one tool rotation. This runs in parallel with a conventional thermal analysis running for the whole weld cycle. The model was tested at two tool rotation speeds with experimental data for three wrought aluminium alloys, and two casting alloys (one aluminium and one magnesium). Heat generation history was found to be remarkably similar for both rotation speeds and across all five alloys. A key aspect of the model is the use of a physically-based kinematic boundary condition at the tool-workpiece interface, with the surface velocity profile having an inner sticking region and an outer slipping region. The method shows the potential for rapid calculation of heat input and temperature fields in large strain frictional processes such as FSSW, without recourse to fully coupled explicit FE analysis.

1. Introduction

Friction stir spot welding (FSSW), shownschematically in Fig. 1, is a potential sheet joining process for automotive applications. A rotating cylindrical tool made from a hard, wear-resistant material, is plunged into two overlapping plates, and retracted after a dwell time of the order of 1 s. This short cycle time and its suitability for thin sheets (~1 mm) make the process a viable alternative to resistance spot welding (RSW) and self-piercing rivets (SPR). Conventional FSSW tools leave a hole, associated with low static strength (Badarinarayan et al., 2007) or cracking (Yamamoto et al., 2007). As a consequence, attempts have been made to eliminate the hole using a refill variant of FSSW (Uematsu et al., 2008), or a pinless tool (Bakavos and Prangnell, 2009; Bakavos et al., 2010).

1.1. Experimental studies of FSSW

Many authors have investigated FSSW experimentally, studying the influence of welding parameters and tool geometry on weld microstructure (grain refinement, formation of intermetallic phases), weld properties (hardness, and failure strength under static and cyclic loading), and tool wear (Yang et al., 2014). A full metallurgical bond requires the depth of the plasticized zone to be sufficient to disrupt the interface between the workpieces, and therefore depends on the heat generated, the temperature field, and the material flow – the focus of this work. Metal flow has been visualised by various techniques. Su et al. (2006) exploited the different etching characteristics in dissimilar spot welds of Al 5754 and Al 6111, and used Al_2O_3 tracer particles in Al 6061 welds, while Lin et al. (2013) used Cu and W powder. In both cases, material movement in the radial and through-thickness directions depended on the tool pin geometry. Gerlich et al. (2006) attempted to infer strain-rate values from sub-grain measurements in Al and Mg alloys. In spite of the low precision, the results suggested full sticking at the tool interface in some alloys, and slippage at the periphery of the tool in others.

Bakavos and Prangnell (2009) and Bakavos et al. (2010) studied FSSW of 6000-series aluminium automotive sheet with various pinless tool designs, demonstrating that successful joints could be produced, assessed via failure loads and energies. In collaboration with this research group, Reilly et al. (2015) presented marker experiments with a pinless tool, using dissimilar Al alloys 6082 and 6111 in a butt configuration, to provide etching contrast. A systematic layering of the alloys from each side of the butt joint was observed, with the number of layers being closely correlated with the number of tool rotations. An analytical kinematic model was proposed, assuming purely circumferential flow. This model successfully predicted the main features of the marker experiments, providing strong evidence for a stick-slip velocity profile at the surface of the workpiece in contact with the tool shoulder.

* Corresponding author.
E-mail address: hrs@eng.cam.ac.uk (H.R. Shercliff).

https://doi.org/10.1016/j.jmatprotec.2018.07.031
Received 21 March 2018; Received in revised form 24 July 2018; Accepted 25 July 2018
Available online 27 July 2018

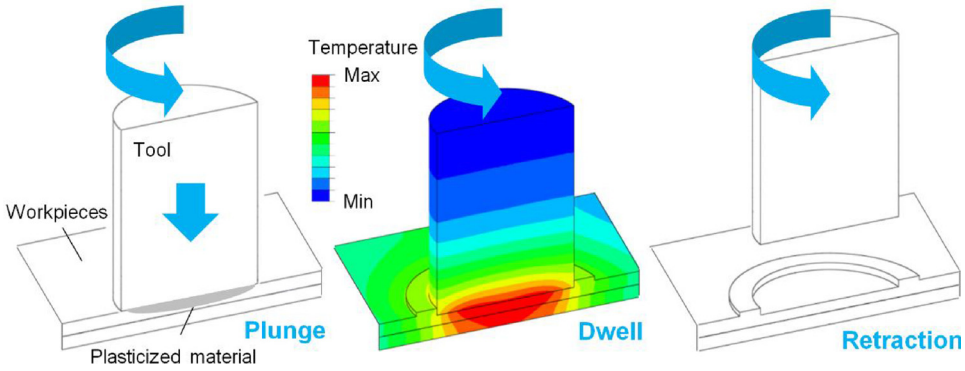

Fig. 1. Friction stir spot welding process.

The physical insight from their work forms the basis of the kinematic boundary condition used in the current model, discussed further below.

1.2. Numerical modelling of FSSW

Several authors have conducted numerical studies of friction stir processes, with the objectives of understanding the process mechanisms, and reducing the number of empirical trials needed to optimise processing conditions, as emphasized by Threadgill et al. (2009). The effect of tool geometry on material flow has been explored by numerical particle tracking, for example by Hirasawa et al. (2010) in FSSW of 6000 series Al sheet. Two alternative approaches to this problem were used by Kim et al. (2010), who simulated FSSW of Al 5083-H18 and 6022-T4 with Lagrangian FEM and Eulerian FVM. Other thermal-mechanical FE models investigate the heat generation and temperature profiles for FSSW of 6061-T6 aluminium alloy, such as Awang and Mucio (2010), and Lacki et al. (2013). The dependence of material deformation and heat generation on rotational speed and plunge rate was investigated by 3D FE analysis by Khosa et al. (2010).

A survey by Neto and Neto (2013) suggests that, whilst most of the modelling work published on friction welding is focused on material and heat flow, only some studies directly link constitutive response to weldability and process optimisation. Examples include: prediction of the rotation speed at which minimum translation force is required in FSW (Colegrove et al., 2007); a study of the influence of tool thread on the welding forces, by the same authors (Colegrove et al., 2007); the relationships between tool forces and speeds, and the strain-rate and temperature-dependent flow stress (Ulysse, 2002); and exploration of the susceptibility to defect formation (Schmidt and Hattel, 2005).

Neto and Neto (2013) also note that current numerical models of friction welding processes often fail to meet the accuracy requirements of practical applications, and are not used to optimize process parameters and significantly reduce experimental trials. Inadequate representation of the material constitutive response in the relevant strain-rate and temperature regimes has been frequently cited as the main source of inaccuracy in model predictions, for instance by Ulysse (2002). The hot constitutive response governs the heat generation and material flow in thermomechanical modelling, linking the deformation behaviour with machine parameters and alloy weldability.

A further prerequisite that is critical for capturing the physics of any thermomechanical model of friction welding is the use of realistic material tool-workpiece contact conditions. Typically, authors assume complete contact and simply apply a Coulomb friction law with an effective friction coefficient – for example, Song and Kovacevic (2003). A calibration method was applied by Frigaard et al. (2001), who adjusted the coefficient of friction at each time-step to control the temperature beneath the tool shoulder. Schmidt et al. (2004) questioned the application of Coulomb friction, considering it unrepresentative for their FSW model, and defined several stick/slip contact states at the tool-workpiece interface. Nandan et al. (2008) agreed that friction coefficient cannot be determined from fundamental principles or by simple experiments relevant to FSW conditions. This applies equally to FSSW, where the contact stresses depend on temperature, material softening, and relative velocity, so experimental measurements can only give apparent average conditions. Temperature and normal stress vary over the tool-workpiece interface, so the contact conditions vary spatially, potentially giving regions of stick and slip, and also vary with time during the process, as noted by Threadgill et al. (2009). Schmidt et al. (2004), in their analytical model of stick/slip contact, made several assumptions: a uniform distribution of the ratio of tool and workpiece velocities, and uniform pressure and shear stress. Colegrove and Shercliff (2005) specified sticking of material to the tool, but with two modifications: the use of a limiting shear stress (Colegrove and Shercliff, 2004) and a calibrated reduction in contact radius, varying between 75 and 100% of the actual shoulder radius (Colegrove et al., 2007).

An alternative method to describing contact in terms of friction and contact stresses is to impose purely *kinematic* boundary conditions instead. Xu et al. (2001) proposed that the workpiece surface rotated at some fixed fraction of the tool rotation speed, in other words with slipping contact over the whole tool. While this has the desired effect of reducing the heat input compared to full sticking, it gives a physically unrealistic discontinuity in velocity at the tool periphery. The approach used in the current study follows the work of Reilly et al. (2015), who inferred the velocity field in FSSW using marker experiments between alloys of comparable strength but dissimilar etching response, and an analytical model. In the present work, surface velocity profiles similar to those inferred by Reilly et al. are directly specified in the model, as boundary conditions.

1.3. Computational efficiency and large deformations

The computational penalty of modelling the complete process in FSSW is great – a direct consequence of the large plastic shear strains in friction welding at high rotation speeds, with steep gradients in strain and temperature with position. This normally implies the necessity for Eulerian or Arbitrary Lagrangian-Eulerian (ALE) analysis, or other remeshing techniques, and very fine meshes, all associated with a significant computational penalty. This creates an obstacle for the adoption of these techniques as routine design tools.

A new finite element method is proposed here to provide a computationally efficient approach for modelling thermomechanical processes such as friction welding, in which deformation and heat flow occur on different time scales. The concept was demonstrated in preliminary form by Reilly et al. (2013), and (Reilly, 2013). The method has potential in large strain frictional processes such as FSSW for rapid calculation of the distribution of heat generation, and the associated temperature field. Reilly et al. also observed that well-instrumented experiments and reliable constitutive material data are prerequisites for thermomechanical process modelling. In this paper, the small-strain

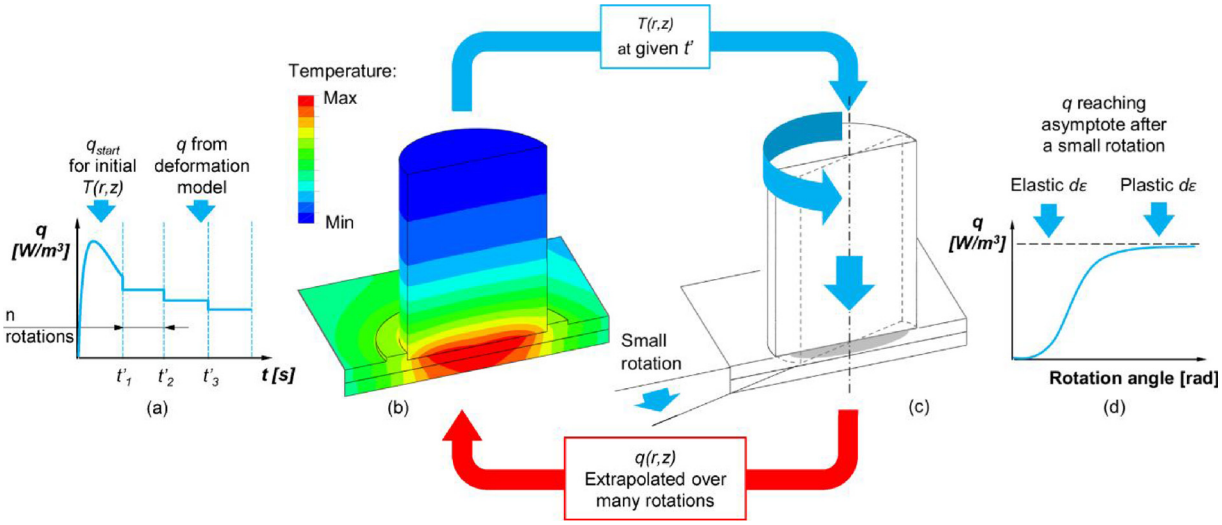

Fig. 2. Small strain analysis of friction stir spot welding: (a) power input $q(t)$; (b) thermal model; (c) deformation model; (d) instantaneous power q from asymptote of deformation model.

modelling concept is implemented for FSSW, with a custom-designed experimental rig for validation of the predicted heat generation.

Principally, this new method uses independent thermal and deformation models, coupled via transfer of the thermal load and temperature field. The main novelty lies in the deformation model, which takes intermittent small strain "snapshots" during the continuous thermomechanical process, but over a much shorter timescale than the interval between deformation analyses. These small strain analyses import the current temperature field, and are sufficient to capture enough of the material flow behaviour to compute realistic values of the plastic strain-rate and flow stress distributions, and thus heat generation. There are two sources of computational efficiency – firstly, the deformation model simulates only a small fraction of the total process time; and secondly, the strain and mesh distortions are small, so that the demanding kinematic description and remeshing associated with large strains is avoided. A schematic of the procedure is shown in Fig. 2.

Within each cycle, the temperature field from the thermal model (Fig. 2b) is imposed as an input to the deformation model (Fig. 2c), which evaluates the spatial and net heat generation rate. Two options are then available: (a) partial coupling, in which an independent measurement of the power history is used as the input to the thermal model, and this is compared with the power predicted by the deformation model; (b) full coupling, in which the predicted power from the deformation model is fed back and used step-wise as the input to the thermal model (as in Fig. 2a). The small strain method works because the deformation analysis only needs to apply sufficient strain to capture the plastic strain-rate and flow stress distribution at the time of the snapshot analysis, and hence to evaluate the consequent heat generation rate distribution (Fig. 2d). The assumption is therefore that the change in temperature between successive analyses produces only a relatively slow change on the material behaviour in the deformation model. Furthermore, as the entire duration of the process is modelled thermally, the temperature field is available at any instant in the weld cycle, which is useful for both experimental validation and microstructure modelling.

Key inputs to the model, presented later, are therefore: (i) the hot deformation constitutive data for each alloy (collated from multiple studies in the literature, and smoothed with best-fit curves); (ii) the contact conditions at the tool-workpiece interface, expressed as a surface radial variation of circumferential velocity. Validation of the thermal field and the predicted heat generation was facilitated by measurements from a purpose-built instrumented rig, which is described next.

2. Experimental work

The geometry of FSSW with a pinless tool is also suitable for studying the fundamentals of the friction processing response of different alloys. First, pure rotation without translation or tool tilt offers a simple experimental procedure, with an axisymmetric flow field; and second, FSSW provides a straightforward geometry for simultaneous measurement of temperature history and applied torque (and hence input power). Greater understanding of the contact and heat generation in FSSW should also inform interpretation of the behaviour in the related processes of rotary friction welding and friction stir welding.

A new instrumented FSSW rig was designed with these aims. Process conditions were similar to those in conventional FSSW lap joints, but autogenous welds were produced using a single workpiece, to focus on temperature evolution, metal flow and heat generation. The rig is able to cover a wide range of temperatures and strain-rates by varying the machine parameters and tool sizes, in order to test the dependence on the constitutive behaviour of a range of light alloys. Full details of the design and its experimental validation are presented by Jedrasiak and Shercliff (2017).

2.1. Autogenous FSSW rig

The experiments were conducted on a TTI RM2 precision friction stir welding machine at TWI Sheffield, which has a maximum rotational speed of 3000 rpm, downforce of 100 kN, power of 37 kW and torque of 500 N m. The machine had an in-built data acquisition system measuring tool forces, speeds and displacements in all three directions, as well as torque and rotational speed. The rig was designed to improve the accuracy of the measurement of torque at the workpiece, and to record temperature at multiple radial positions within the workpiece. Flat pinless tools of diameters 10, 16 and 19 mm were tested. The results here all relate to the 10 mm tool, as used in previous experimental and numerical work by the current authors (Jedrasiak et al., 2016) and in the FSSW trials by the collaborating research group (Bakavos and Prangnell (2009); Chen et al. (2013)). Identical tooling was also used in the underpinning alloy marker experiments, carried out by Bakavos et al. (2010) and Reilly et al. (2015).

A 50 × 45 mm sample of thickness 6 mm was chosen to accommodate tools up to 16 mm in diameter and a deformation zone up to 1 mm deep. From the modelling perspective, it was preferable for the sample to provide a sufficiently large heat sink, and to keep the workpiece-backing plate interface at a reasonable distance from the

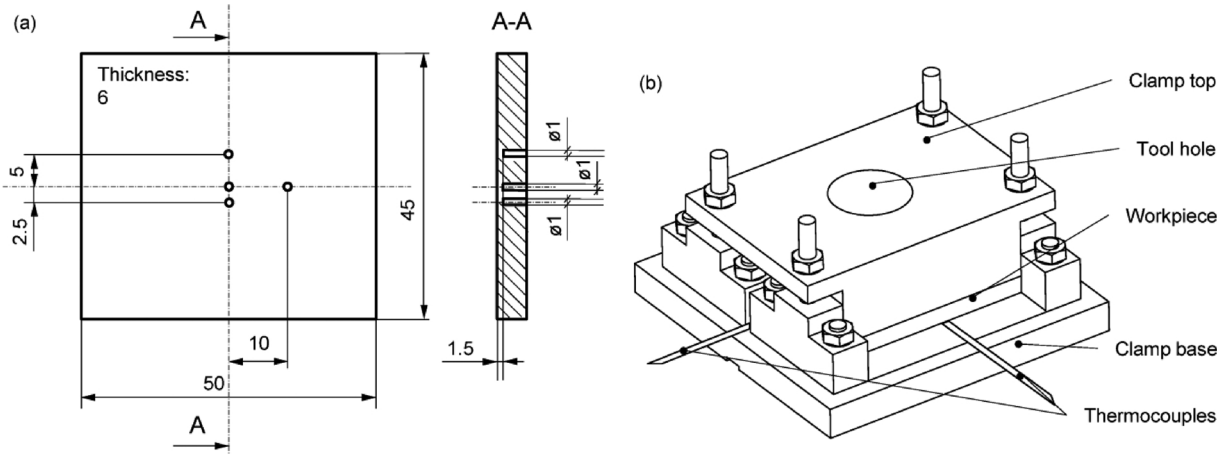

Fig. 3. Details of the experimental rig: (a) plan and section view of a sample and thermocouple locations (dimensions in mm); (b) complete workpiece and clamp assembly.

deformation zone (to reduce sensitivity to heat transfer conditions). Standard *k*-type thermocouples of diameter 0.5 mm were located in drilled holes as close as possible to the deformation zone, with the tips 1.5 mm from the top surface (Fig. 3a). Accurate positioning of thermocouples was required, given the large through-thickness temperature gradients reported by the current authors (Jedrasiak et al., 2016).

The workpiece and clamp assembly is shown in Fig. 3(b). Thermal losses between the workpiece and clamp was limited via ceramic inserts in the steel clamp top and base, such that the steel parts of the clamp were separated from the workpiece by a small air-gap. The thermocouple wires were located in grooves in the ceramic insert in the base, to ensure the thermocouple tips were pushed firmly against the workpiece material. The assembly was mounted on a commercial load cell, custom-built by Sensing Systems Corporation, designed to accommodate 80 N m torque and 30 kN axial load, with nominal combined errors smaller than 0.35% of torque capacity and 0.25% of axial load capacity. A simultaneous NI 9237 bridge module was used to log torque and load at a sampling rate of 50 Hz. Thermocouple measurements were made with an analogue input NI C-series module, at the same sampling rate. The load cell and clamp-workpiece assembly was attached to the machine bed. The centre of the rig was aligned carefully with the axis of the tool in the machine head, to ensure that the thermocouples were located accurately at their target radial locations.

2.2. Test conditions

The optimum configuration of clamps and thermocouples was determined in an extensive range of trials, also testing the reliability of the rig and its instrumentation (Jedrasiak and Shercliff, 2017). These trials explored the sensitivity of the key outputs (downforce, torque, and temperature) to variation in the process variables (tool diameter, plunge depth and rate, rotation speed, and dwell time). An optimum set of thermocouple configurations was established, and a standard set of process conditions, shown in Table 1. A plunge depth of 0.2 mm was chosen to minimise the change in geometry, while ensuring full tool-workpiece contact and reproducible stick-slip conditions. At the nominal plunge-rate of 20 mm/min, the plunge should take 0.6 s, but in practice the full plunge was achieved in a time closer to 2 s, due to the resistance of the initially cold material. A dwell time of 30 s is unrealistic in practical processing terms, but was adopted to provide near steady-state conditions under the tool, for modelling purposes. The modelling methodology was first developed for the lower speed of 500 rpm using medium strength wrought Al alloy 6082-T6 and then extended to 2000 rpm, before testing at both speeds on 4 alloys of contrasting composition and as-received strength: medium and high strength wrought Al alloys 2024-T3 and 7449-T3, and two casting alloys: AlSi10Mg, and Mg-Al alloy AM50.

Table 1
Welding parameters.

Parameter	Value
Material	6082-T6, 2024-T3, 7449-T3, AlSi10Mg, AM50
Sheet thickness	6 mm
Tool diameter	10 mm
Plunge depth	0.2 mm
Plunge rate	20 mm/min
Dwell time	30 s
Rotation speed	500 rpm, 2000 rpm

2.3. Experimental results

Torque histories for the five alloys are shown in Fig. 4(a and b). Across the four Al alloys there are differences in peak torque and the rise time to the peak, but the decaying parts of the curves are similar. At 500 rpm, the torque peaks within the first 5 s, and then decays exponentially, to a value around 20–25% of the peak. At 2000 rpm, the peak torque is lower by a factor of about 2, and occurs within 1–2 s, again falling exponentially to a value around 20–25% of the peak. At both speeds, the torque with the Mg alloy is consistently lower. The variation in peak and rise time suggests that the plunge time is dependent on the differences in material strength.

The downforce histories recorded in the same experiments (Fig. 4c and d) show some similarities to the torque histories, but there is more variation between the materials. The higher strength alloys 2024 and 7449 show similar downforce curves, as do the medium strength 6082 and AlSi10Mg casting alloy. The Mg alloy AM50 results do not follow such a consistent pattern.

These measurements of torque and downforce were compared with those from the machine (Jedrasiak and Shercliff, 2017), and showed a similar profile with time, giving confidence in the use of the rig on other machines without instrumentation. The torque is the determining factor in heat generation, so this is most important for validation of the modelling work.

The corresponding temperature histories at the weld centre are shown in Fig. 5. It is notable that the temperature histories for the different alloys are remarkably similar, which is consistent with broadly similar heat input, suggested by the torque curves (allowing for some differences in thermal properties between alloys). Note that in all cases the temperatures show an initially steep rise within 5 s at 500 rpm, and 2 s at 2000 rpm. The curves then turn and only rise by another 50 °C over the remainder of the 30 s dwell time. The peak in torque is thus

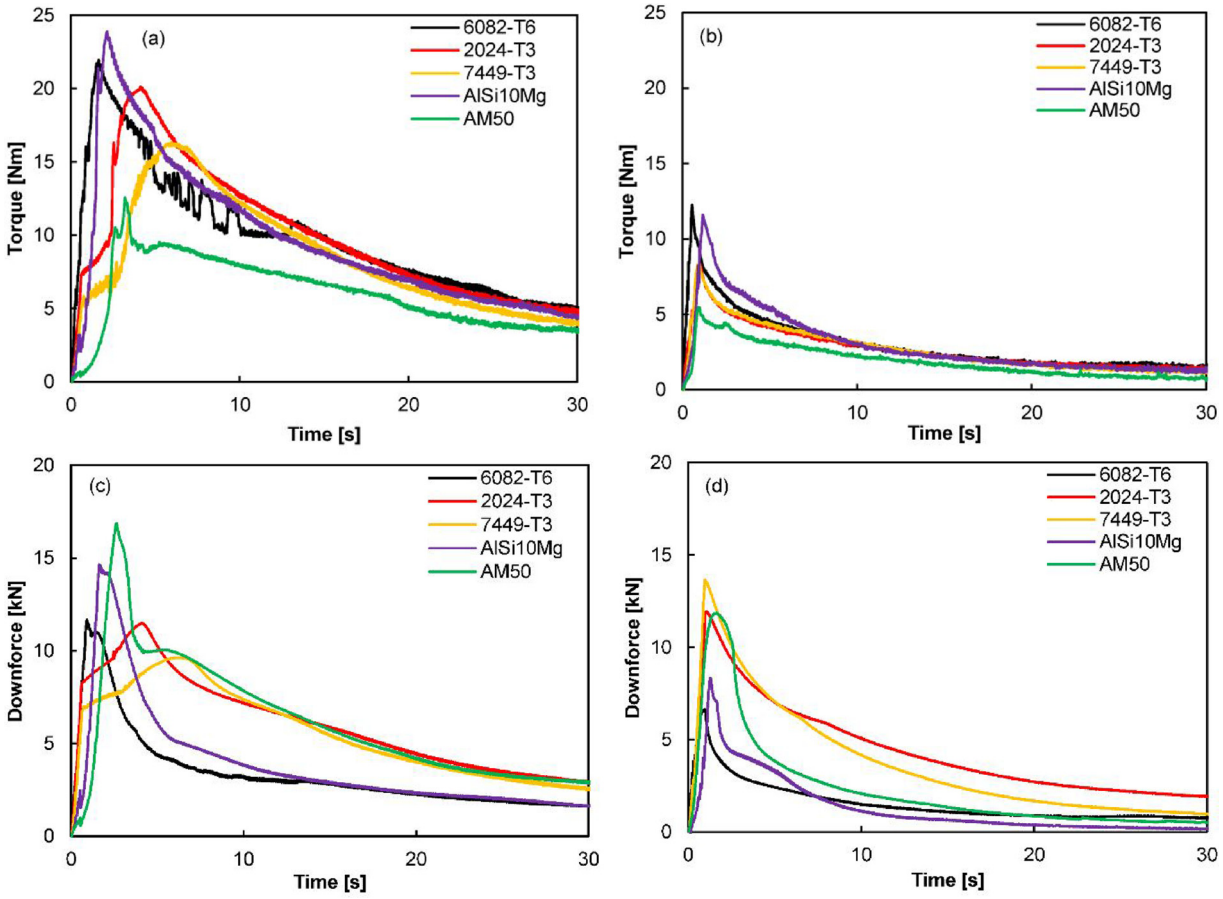

Fig. 4. Torque and downforce as a function of time, for different alloys, at: (a,c) 500 rpm; (b,d) 2000 rpm.

associated with the end of the initial steep temperature rise. The initial steep rises in torque and temperature appear to be consistent with the plunge period, but at deeper plunges and higher plunge rates, the curves did not show this correlation.

3. Thermal model

3.1. Mesh and geometry

The thermal model applied in this work is adapted from that presented previously by Jedrasiak et al. (2016). The adaptations needed to apply the model to the new rig are summarised here. Fig. 6(a) shows the layout of the FE thermal model, consisting of about 55 thousand 8-node linear heat transfer brick elements. Only the two ceramic elements of the clamping assembly in contact with the workpiece are included in the model – due to their low thermal conductivity, heat conducted through these parts to the remaining elements of the assembly can be neglected. A full 3D thermal model was used, as the temperature distributions are later imported to the deformation model, which captures the predominantly circumferential material flow.

Implicit time integration was used. The load transfer procedure, used for coupling the separate analyses of the temperature and

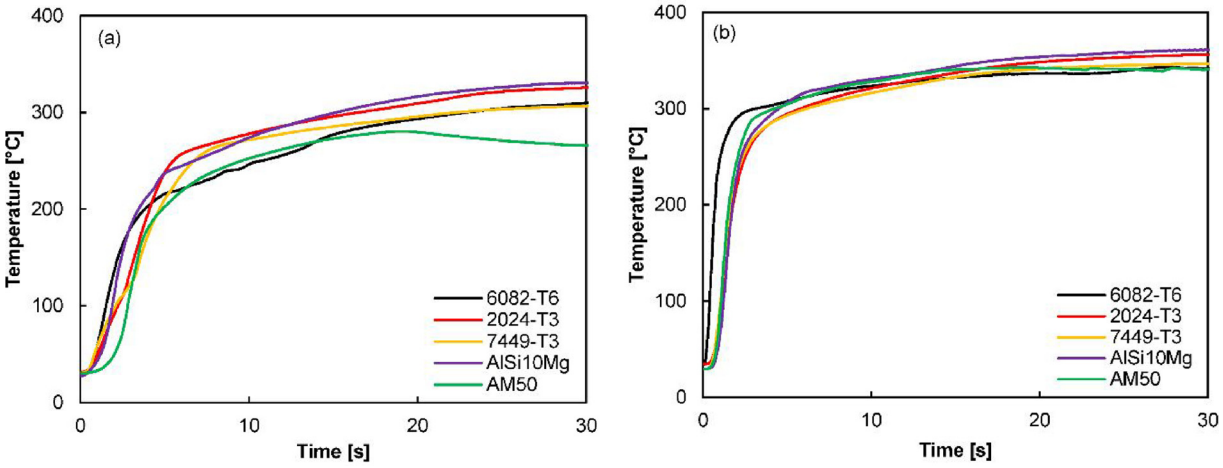

Fig. 5. Temperature histories at the weld centre, for different alloys at rotation speeds of: (a) 500 rpm; (b) 2000 rpm.

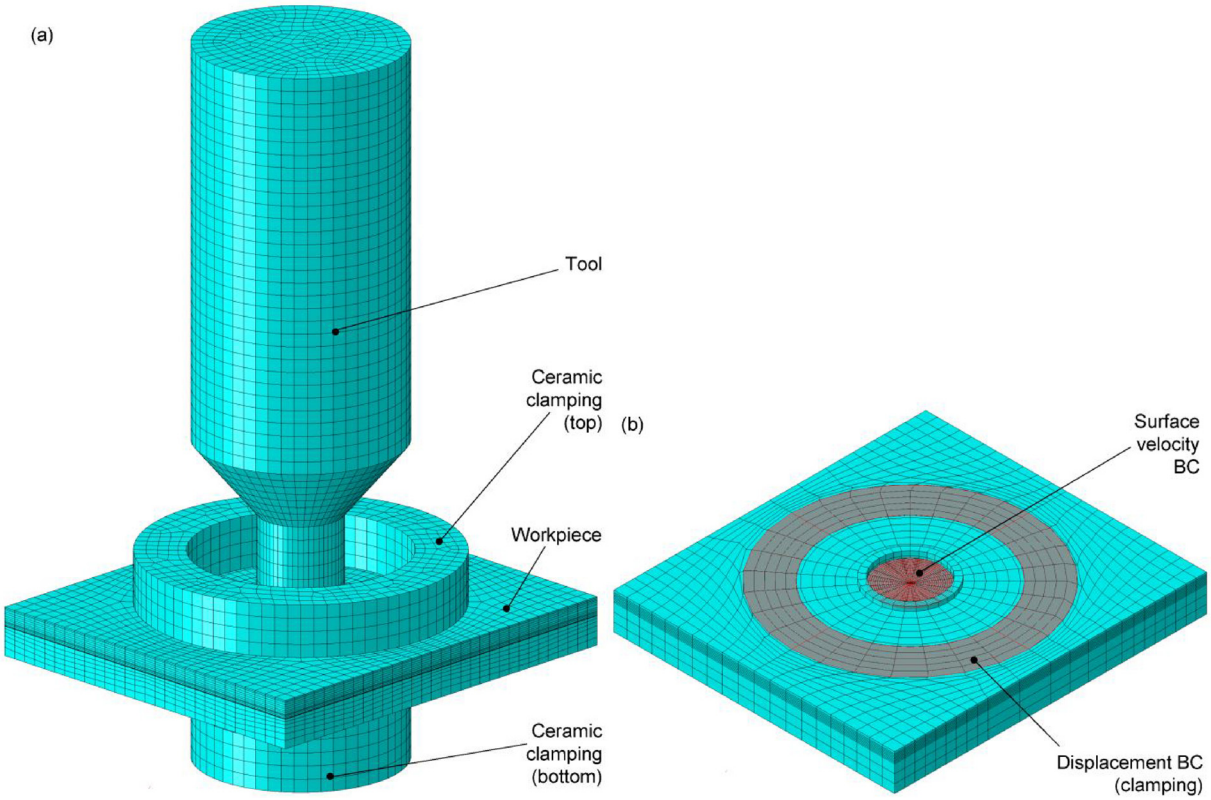

Fig. 6. Geometry, meshes and boundary conditions (BC) for FE analysis of autogenous FSSW: (a) thermal model; (b) deformation model.

deformation fields, offers several advantages, e.g. the possibility of using dissimilar meshes, and different procedures of time integration. While explicit time integration might be more efficient in the deformation model, the implicit method is unconditionally stable for linear problems, and in heat transfer problems non-linearities associated with the temperature-dependent material properties or boundary conditions are usually mild.

The plunge stage presents a particular problem in modelling FSSW, since the thermal model required the tool location and associated heat input to be fixed. In reality, at the plunge rate used in the current experiments, a depth close to the maximum was reached about 2–3 seconds after initial contact, and increases slightly throughout the subsequent dwell time, as the material softens and the tool penetrates the surface. Sensitivity analysis in an earlier study by Jedrasiak (2012), found that the evolving plunge depth had secondary importance on the predicted thermal field, for plunges up to 0.5 mm in a sample of thickness 2 mm. The model plunge depth was therefore set equal to the final depth, as measured experimentally. Flash around the tool was included in the model, with the geometry simplified to a ring, and dimensions measured experimentally.

3.2. Materials and boundary conditions

Material properties (thermal conductivity, specific heat and density) were specified as temperature dependent, due to the significant variation within the analysed temperature range of 20–400 °C. Thermal property data are presented in Fig. 7 for all five test alloys (as listed in Table 1). Where appropriate material data were not available, they were assumed to be the same as those for a similar alloy, e.g. thermal data for Al alloy 7075 was used as a substitute for 7449. In some cases data were only available for part of the relevant temperature range, and was extrapolated over the remaining part of the regime, following the trend in other similar alloys. The properties of the Macor ceramic clamping material (Corning SAS, 2012) and tool steel H13 (Shabgard et al., 2016) were also specified as temperature-dependent, though they varied to a smaller degree.

In the previous FSSW model, all surfaces in contact with the air were treated as insulated, which was justified by the short FSSW cycle time of 1 s (Jedrasiak et al., 2016). Here, due to the longer dwell time of 30 s, a fixed convection coefficient of 100 W/m^2K was specified, after Dickerson et al. (2003). Due to the high contact pressures and workpiece softening, perfect thermal contact was assumed at all interfaces between the workpiece and the tool or ceramic clamping elements. Tool retraction was not included, as the thermal history was only needed during plastic deformation, and not for the cooling stage.

3.3. Thermal loads

The thermal FE model uses the spatial distribution for an identical tool and welding conditions, as in Jedrasiak et al. (2016). Radially, a triangular heat input profile is applied, with a peak value at 0.75 of the tool radius (Fig. 8). This reflects the surface velocity profile inferred by Reilly et al. (2015) from marker experiments and a kinematic model, discussed further in the deformation model below. It is indicative of sticking contact in the central region of the tool, with the velocity falling to zero close to the tool edge (for continuity with the surrounding stationary material) giving slipping contact around the periphery. Jedrasiak et al. (2016) found that it was difficult to distinguish between surface heating and near-surface volumetric heating, with the temperature field being largely independent of the proportions. A 50% surface/50% bulk distribution is assumed, with the volumetric heat input extending uniformly through a weld zone depth of 1 mm, typical for welds using a 10 mm diameter tool (after Reilly et al., 2015).

The net power history $q(t)$ was calibrated using the method proposed by Jedrasiak et al. (2016). At each time-step, the value was adjusted until the model matched the measured temperature for the thermocouple at the weld centre, giving a piece-wise linear variation in power. The time-step varied between 0.2 s to 5 s, to keep each

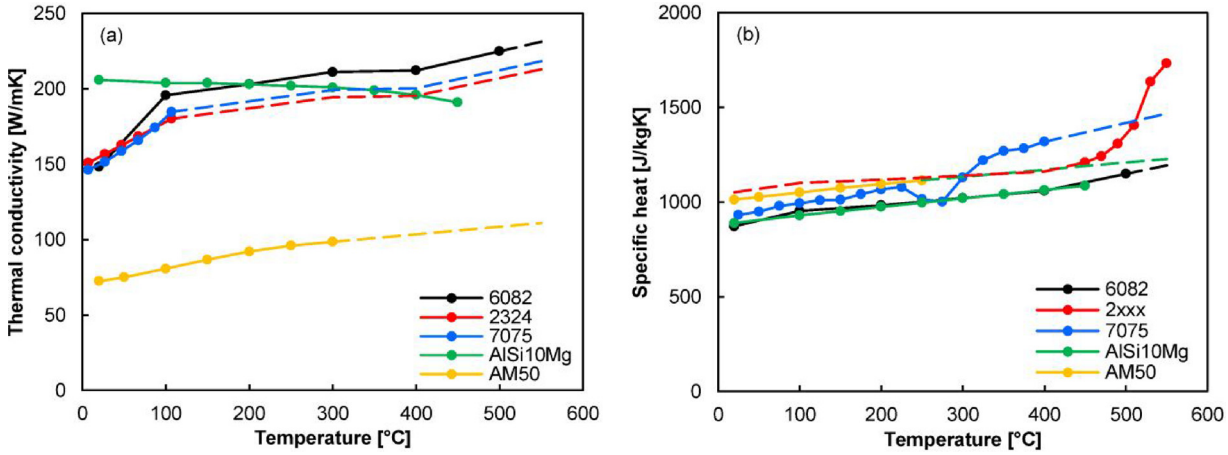

Fig. 7. Properties of workpiece alloys as a function of temperature (datapoints – dots; extrapolated values – dashed lines): (a) thermal conductivity; (b) specific heat; (sources: Nagaumi et al. (2008); Rudajevová et al. (2003); Peel et al. (2006); Kaschnitz et al. (2014); Karthikeyan et al. (2010)).

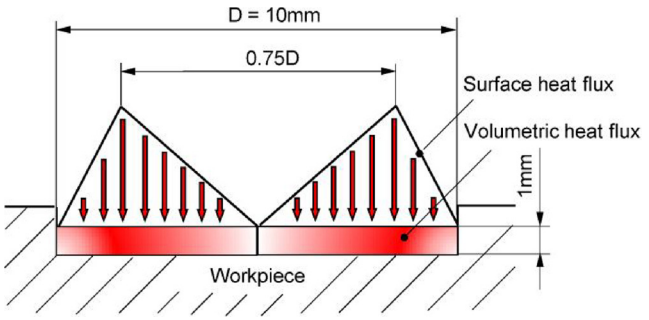

Fig. 8. Thermal loads: radial distribution.

temperature increment below an acceptable level. These "reverse-engineered" power histories are then compared with the experimentally measured power (equal to torque × rotational speed in radians/second). This approach has two advantages over using the experimentally measured power directly as input: (a) reliable thermocouple data are more commonly available than power; and (b) it minimises the error in the temperature predictions, which are carried forward to the subsequent deformation modelling, in which there is a strong temperature-dependence of the flow stress.

3.4. Thermal modelling: results

Fig. 9(a) shows an exemplar set of measured and predicted temperature histories (for Al 6082-T6 at 500 rpm). Overall, a good match was achieved for all thermocouple locations, and similar agreement was found for all five materials at both speeds, as presented elsewhere (Jedrasiak, 2017). Fig. 9(b–f) show the calibrated and measured power histories for the five alloys at welding speeds of 500 and 2000 rpm. In all cases, the predicted power histories are close to those calculated from the experimentally measured torque, though are sometimes under-estimated near the peak.

An important and surprising observation can be made, that was not apparent when directly comparing measured torques (Fig. 4a and b): the experimental power after the peak is practically independent of the welding rotation speed in all five alloys (Fig. 9b–f). As postulated by Mishra and Ma (2005), and by Threadgill et al. (2009), friction welding contact conditions are self-stabilizing, that is, as temperature rises towards the solidus, the flow stress falls and heat generation reduces, so conditions converge on a state of thermal balance. But it is surprising that across five diverse alloys, with a factor of four in rotation speed, conditions converge on such similar heat generation rates. The deformation model, below, is used to shed further light on the prevailing deformation conditions in each alloy.

4. Deformation model

Material flow is modelled with a small-strain approach, where deformation is simulated at several discrete time intervals (Fig. 2), greatly reducing the computational cost, as discussed earlier. At each time corresponding to a snapshot computation, the temperature field is imported from the thermal model and remains unchanged. During each snapshot, rotational displacement is applied from an initially unloaded state, with a step change to the imposed interface rotation speed. Deformation is initially elastic, but is continued until plastic deformation dominates, and the plastic power dissipation asymptotically reaches a constant rate (as in Fig.2(d)), that is, the same as would apply in continuous rotation. The typical rotation required to reach this condition is of order 1°, which explains how the continuous heat generation can be calculated using a small strain implicit analysis with low mesh distortion. Partial coupling is adopted here, with the net heat generation rate, predicted at discrete intervals, being compared with the power history inferred from thermocouple data (from the thermal model), and with that measured experimentally.

4.1. Geometry, mesh and materials

The deformation in friction stir welding is dominated by axisymmetric shearing of the workpiece material. This is modelled here in 3D (Fig. 6b), since the small-strain deformation model imports the temperature field from the thermal model, so the workpiece geometry must be identical (Fig. 6a). Only material flow in the workpiece is of interest, and heat flow is not considered, hence all other parts are excluded from the model, improving computation efficiency. As in the thermal model, the tool plunge depth is assumed constant throughout the entire weld time.

The mesh consists of approximately 16,000 8-node thermally coupled brick, linear displacement and temperature elements. The mesh is finest within the thermomechanically affected zone, where elements with thickness of 0.1 mm were necessary to capture the steep through–thickness gradient in shear strain. The number of elements in the workpiece was reduced compared to the thermal model, to speed up the computation. In contrast to the thermal problem, even a small strain snapshot of plastic deformation was highly non-linear, and convergence with the applied implicit time integration was not as rapid.

4.2. Material constitutive response

Elastic properties were specified as temperature-dependent. If data

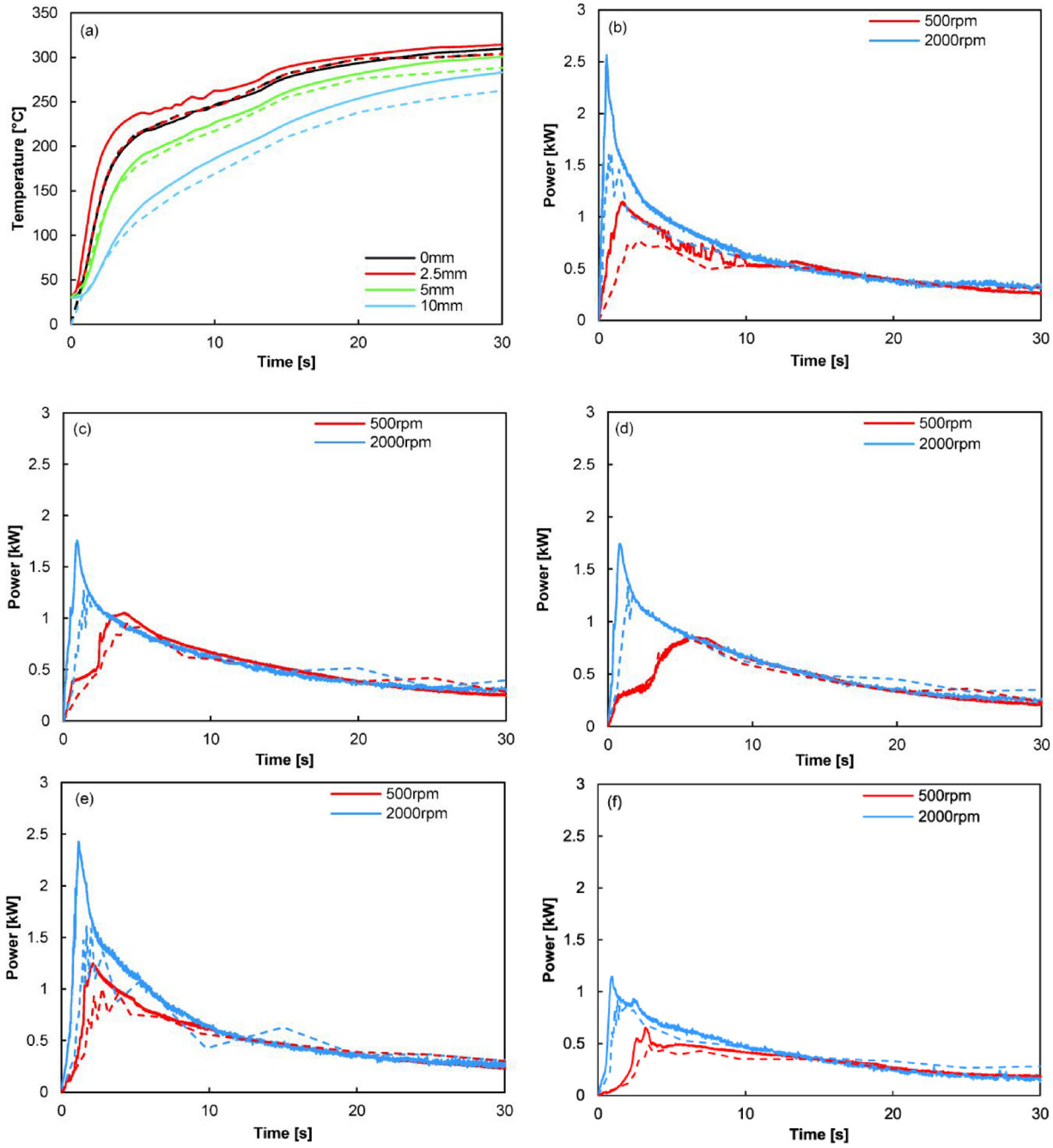

Fig. 9. (a) Predicted (dashed) and measured (solid) temperature histories at different distances from the weld centre, for Al 6082-T6 at 500 rpm. (b–f) Power history inferred from the thermal model (dashed) and measured (solid), for tool rotation speeds of 500 and 2000 rpm, in alloys: (b) Al 6082-T6; (c) Al 2024-T3; (d) Al 7449-T3; (e) AlSi10Mg; (f) Mg AM50.

for the alloys tested were not readily available, Young's modulus and Poisson's ratio for similar aluminium and magnesium alloys were used. These properties have a minimal influence on the results of the small-strain analysis.

In friction stir spot welding of aluminium or magnesium, deformation takes place primarily at high temperatures of order 300–450 °C, where little strain hardening is observed, and isotropic hardening can be neglected. A single-point yield plasticity model favours the proposed small-strain approach, since isotropic hardening requires tracking of the instantaneous position on a stress-strain curve for each element in the model, throughout the entire weld cycle.

In practice, flow stress data is usually available in the literature only for strains much smaller than those observed in FSSW. Hence in each case the stress at the maximum recorded strain (typically equal to 1) was taken as the single-point yield stress, for a given temperature and strain-rate. Data were collated for the alloys tested, or for similar alloys where there were gaps in the data. For this reason, and because of experimental uncertainties, the collated data show some inconsistencies in both temperature and strain-rate dependence. A least-squares best-fit curve was obtained for a mid-range strain-rate, using a polynomial relationship between yield stress and temperature. The yield stress at other strain-rates was then found by assuming a linear scaling relationship between stress and log(strain-rate). At temperatures approaching the solidus, a linear drop to zero flow stress at the solidus was assumed, following Colegrove et al. (2007). The resulting constitutive models are summarized with the underlying data in Fig. 10,

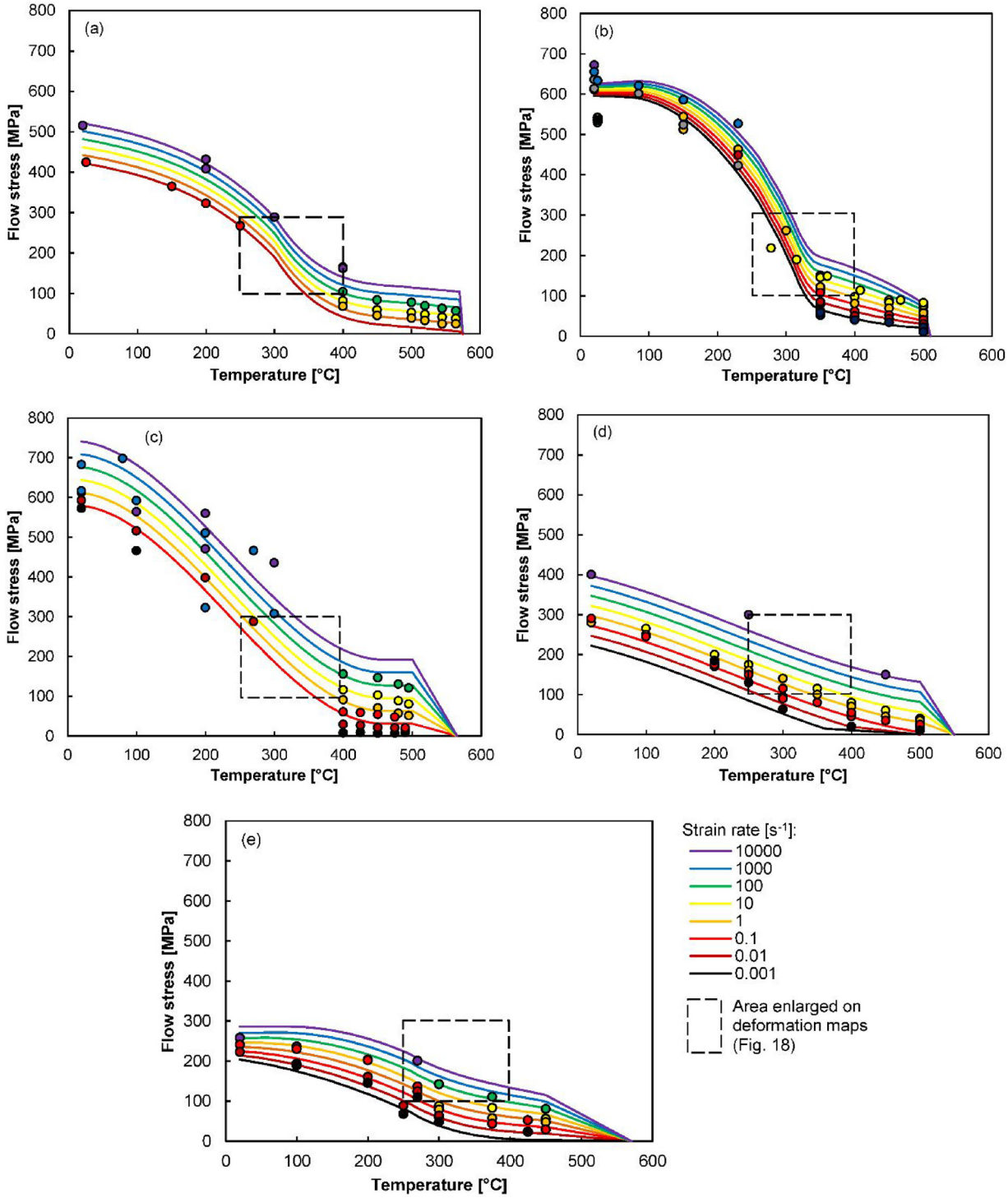

Fig. 10. Constitutive model (solid lines) and underlying yield stress – temperature data (datapoints) for five test alloys, for a range of strain-rates: (a) Al 6082 (sources: Malakizadi et al., (2016); Jaspers (1999)); (b) Al 2024 (sources: Tello et al., (2010); Khan and Liu (2012); Lesuer (1999); Seidt and Gilat (2013); Rodríguez-Martínez et al. (2011); Chen et al. (2015); Bhimavarapu et al. (2011); Wang and Jiang (2012), Cepeda-Jiménez et al. (2012) ; (c) Al 7449 (sources: Chen et al. (2016); Mylonas and Labeas (2014); Wang et al. (2010); Kumar et al. (2009)); (d) AlSi10Mg (sources: Estey et al. (2004); Zamani et al. (2015); Roy et al. (2012); Gupta et al. (2014)); (e) Mg AM50 (sources: Ding et al. (2010); Song et al. (2009); Bae et al. (2002); Slooff et al. (2010); Sanjari et al. (2012); Somekawa et al. (2005); Zhao et al. (2010); Takuda et al. (2005); Lingyun et al. (2006)). (The dashed boundaries mark the ranges of σ and T shown enlarged in later material deformation maps, Fig. 18).

highlighting the significant spread in initial room temperature strengths.

Note that the use of this collated data is in marked contrast to the approach that is common in the literature, which is to assume the validity of a Johnson-Cook model (Johnson and Cook, 1983) or Zener-Hollomon equation, with parameters fitted to the response over a limited range of temperature and strain-rate. This ignores the shortcomings of both material models when applied to friction welding, as emphasized by Grujicic et al. (2012). In spite of the more complex deformation analysis that is often conducted in modelling friction processes, insufficient attention is often paid to the validity of the input data.

4.3. Loads and boundary conditions

The workpiece is subjected to forces resulting from frictional contact with a rotating tool, plunged into the workpiece under a large downforce. Whilst the net torque and downforce histories are known experimentally, the spatially- and time-varying contact pressure and shear stress conditions are not.

The approach presented here follows the work of Reilly et al. (2015), who noted that the deformation zone is heavily constrained kinematically, and inferred a physically meaningful velocity field using marker experiments. Their novel analytical approach showed that the layering observed between dissimilar alloys in a butt weld configuration could be interpreted by a radial variation in stick-slip conditions at the tool-workpiece interface, with the central region of the workpiece sticking to the tool, and a slip region towards the outer periphery. The kinematic model predicted the relationships between the surface velocity profile and weld time, with the shape of the deformation zone and the variation in layer thickness with depth. In the present work, a more refined approach is taken, with the surface velocity profile being inferred directly from their weld cross-sections. (Reilly et al., 2015) made welds with speeds ranging from 300 to 2000 rpm, but did not include experiments at 500 rpm, so the velocity profile at 500 rpm was assumed to be identical to that at 800 rpm, scaled in proportion to the rotation speed.

Fig. 11 shows a schematic view of the layering observed in dissimilar FSSW butt joints, and illustrates the method used to obtain the distribution of velocity in both radial and through-thickness directions. In the central region, the maximum number of (double) layers corresponds to the total number of revolutions which occur during the weld time, assuming sticking occurs instantaneously at the start of welding (confirmed as a reasonable approximation by Reilly et al. (2015)). Each layer corresponds to half a revolution at the surface, so the *average* circumferential velocity at each layer boundary increases in integral steps up to the surface. This is illustrated in Fig. 11, for vertical sections in the central and peripheral regions. Since the time elapsed is the same for all locations, the average rotational *angular* speed can therefore be found for each point. Repeating this process at different radial positions, and finding the maximum rotational speed at the surface in each case, generates the *radial* profile of angular and circumferential velocity at the tool-workpiece interface, as shown in Fig. 12a. In all cases, a plateau of angular speed is observed over a central part of the tool, corresponding to sticking conditions in the domain where the layering is horizontal. Where the material rotates more slowly than the tool, slip occurs, and the layering curves towards the surface, and the number of layers in the vertical direction falls to zero at the tool periphery. The *actual* surface circumferential velocity profile can then be obtained directly by multiplying the rotational speed by the radial distance – the result is shown in Fig. 12(a and b), giving a linear rise in velocity in the central sticking region (over which the rotational speed is constant, i.e. $v = \omega r$).

As the tool-workpiece contact is specified kinematically, at a fixed plunge depth, the downforce is not included in the model. The stresses resulting from the downforce are predominantly hydrostatic, as the weld zone is heavily constrained by the cold surrounding material and clamping. The downforce does not therefore contribute significantly to material yield, and has little influence on generated heat, which is primarily the product of shear stress and strain. The clamping loads on the workpiece also have no influence on material flow and heat generation in the deformation zone, so the clamping was simply modelled by fixing all of the degrees of freedom of the workpiece surfaces in contact with the ceramic clamping components (Fig. 6b).

5. Results and discussion

The small-strain snapshot model is validated using two measures of the power history against time: (a) experimental values of machine power, from the rig torque; (b) heat generation inferred from the FE thermal model, and calibrated against thermocouple data. The time interval between snapshot models was defined as a period of time during which the temperature recorded by the centrally located thermocouple changed by 20 °C, but no larger than 5 s. This limit the scale of the updates to the thermal field, avoiding large discontinuities in predicted power.

The heat generation rate was first predicted for one of the alloys, Al 6082-T6, for both rotation speeds, using the inferred surface velocity profile from marker experiments, as in Fig. 12(b). Fig. 13 shows that the overall shape of the power histories predicted by the deformation model corresponds with the reference power from experiment or thermal model. After an initial peak in power, the material progressively heats and softens, which gives an approximately exponential decay in power. The magnitude of the power, however, is significantly over-predicted, particularly at 2000 rpm (note the different scales in

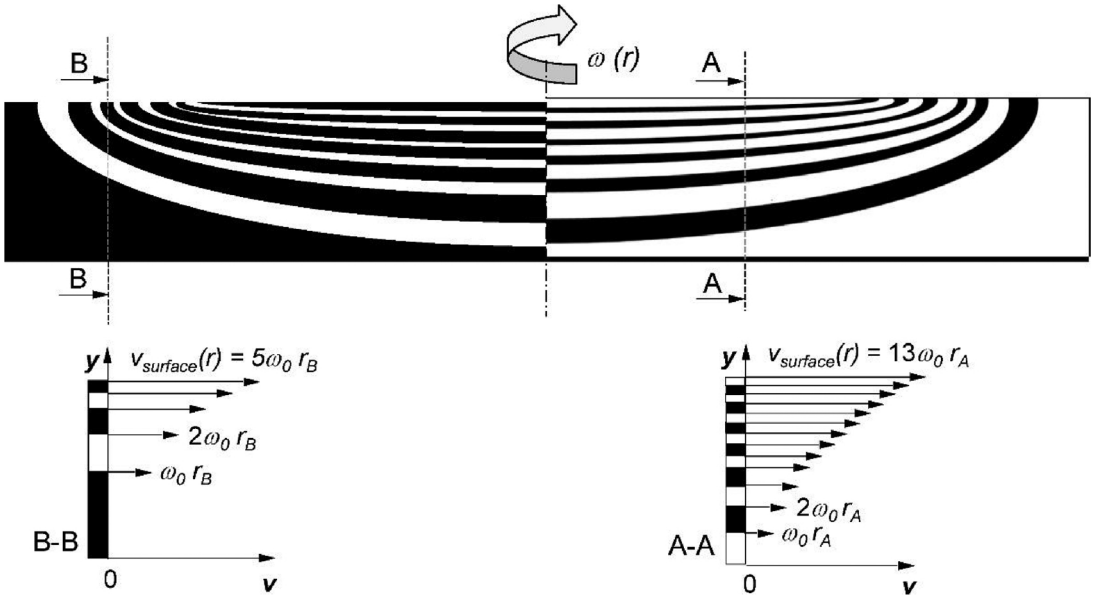

Fig. 11. Schematic view of the layering observed in dissimilar alloy FSSW butt joints, showing the process for inferring the average circumferential velocity profile with depth, for two radial positions.

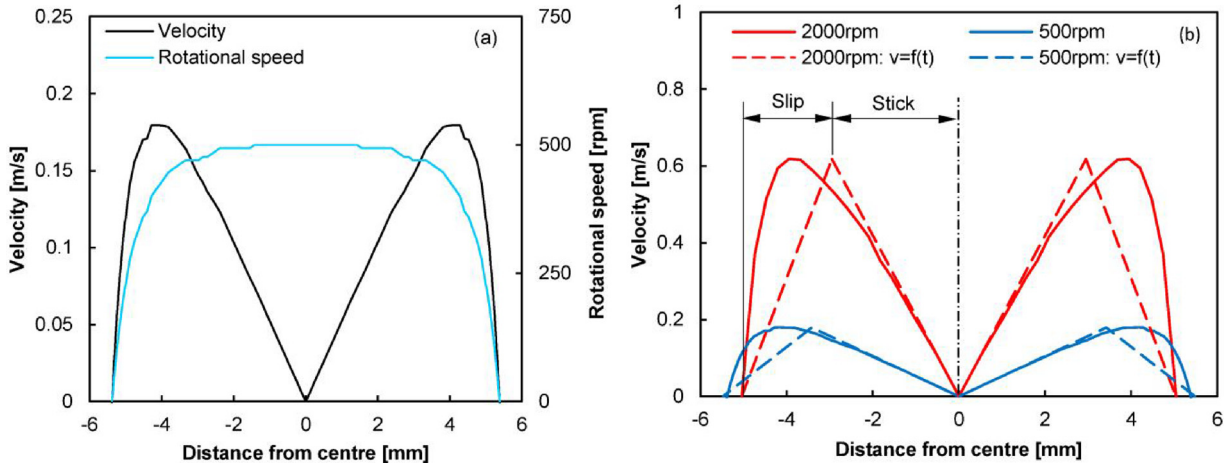

Fig. 12. (a) Radial distributions of rotational speed (angular velocity) and circumferential velocity of material at the tool-workpiece interface, inferred from marker experiments; (b) Radial distributions of the material velocity at the tool-workpiece interface, for two rotation speeds (solid lines show the variation inferred from marker experiments; dashed lines show a linearised approximation).

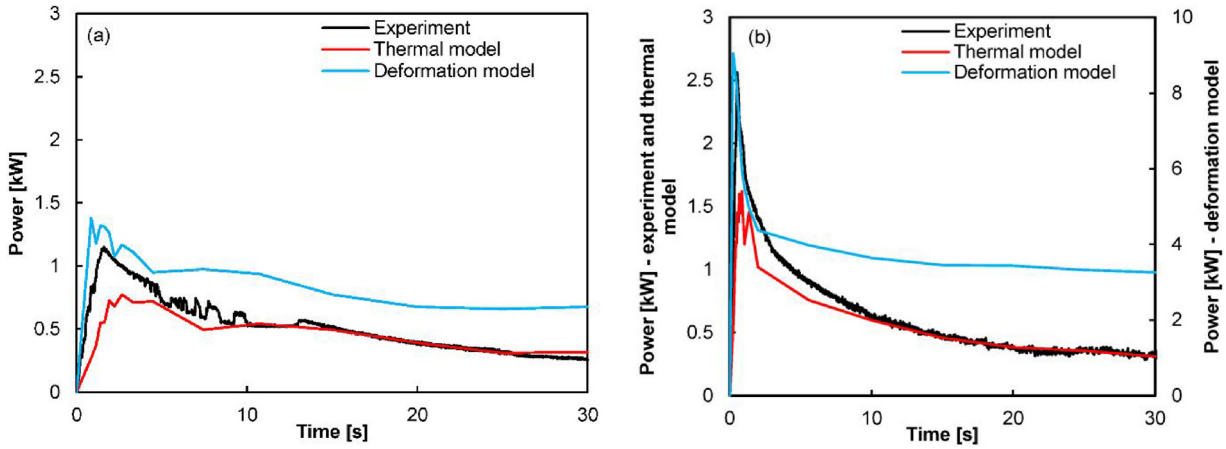

Fig. 13. Predicted power history from the deformation model for wrought Al 6082-T6 at (a) 500 rpm, and (b) 2000 rpm, compared with experimentally measured power, and that inferred from the thermal model.

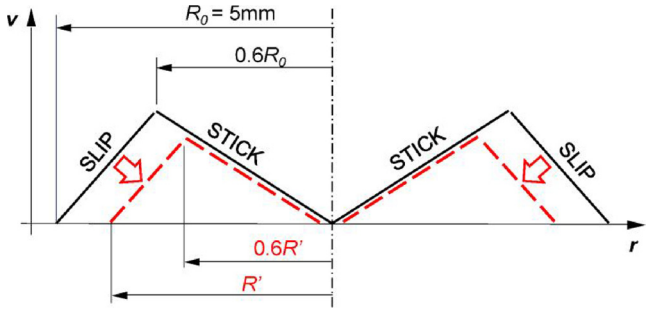

Fig. 14. Empirical adjustment of radial distribution of the surface material velocity at the tool-workpiece interface.

Fig. 13(b)). The same pattern was found in the other four alloys (Jedrasiak, 2017), raising questions about the validity of the method, and requiring a more detailed investigation.

The error in prediction could potentially have three sources: the material model, the temperature field, or the boundary conditions. Other factors such as mesh size may be ruled out, as this was optimised in a sensitivity study (Jedrasiak, 2017). No distinction could be made between the accuracy of predictions across the five alloys – the trend was the same in all cases. This consistency in the errors in power prediction suggests that it was not due to inaccurate material constitutive data, which would be expected to give variable uncertainty from alloy to alloy. Temperature was also ruled out as the main source of error, since the accuracy of the FE thermal model was well-established, and the discrepancy would not be systematic across all five alloys. It was also apparent that the temperature recorded in the weld zone did not approach the solidus temperatures for any of the alloys (between 510 °C and 570 °C). This leaves the relationship between contact conditions, rotational speed and power generation. A simple inference from the model would be that a factor of 4 increase in rotational speed would be expected to result in approximately a factor of 4 increase in power (at comparable flow stress). But in reality, as discussed in Section 4, the experiments show that the power converges on a remarkably similar value regardless of the rotational speed, with relatively little variation between the alloys.

The weld marker experiments of Reilly et al. (2015) gave good insight into the material velocity at the tool-workpiece interface, but only for welds taking 1 s. The velocity profiles of Fig. 12, inferred from these experiments, were used throughout the entire 30 s simulated by the deformation model. In reality, this velocity profile may evolve with time. The area within which material sticks to the tool is limited by friction, which can be expected to change with the downforce. As the downforce decays with the weld time (Fig. 4c and d) sticking may become progressively more limited. In order to test the hypothesis, a study was conducted to investigate the influence of the velocity profile on the predicted heat generation rate.

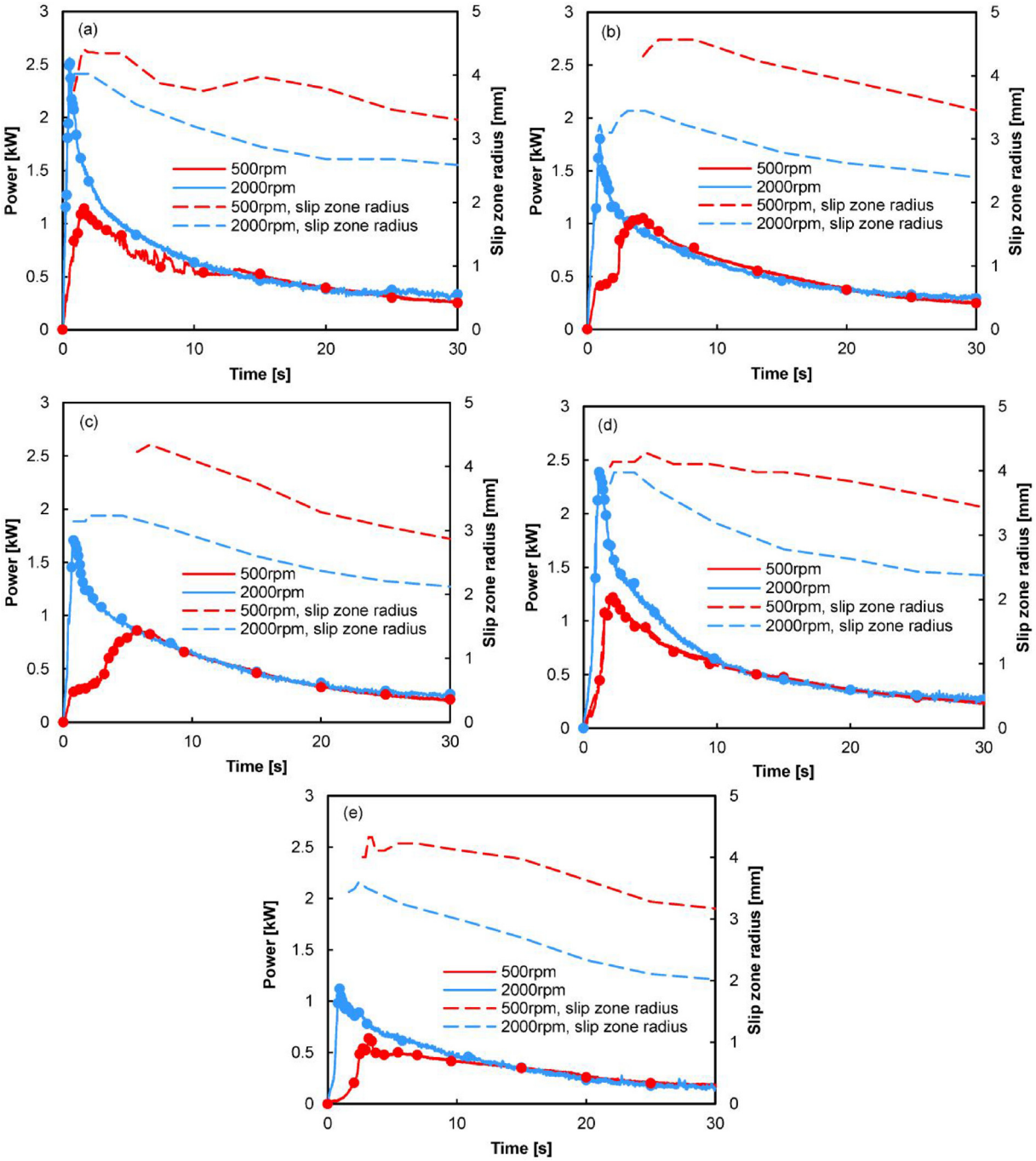

Fig. 15. [LH axis] Predicted power histories from the deformation model (solid circles) for welds at 500 and 2000 rpm, calibrated to the experimentally measured power (solid line), for: (a) Al 6082-T6; (b) Al 2024-T3; (c) Al 7449-T3; (d) AlSi10Mg; (e) Mg AM50. [RH axis] The dashed lines show the variation of the outer radius of the slip zone, R'.

In this iteration of the model, the problem was inverted and used to 'reverse engineer' a velocity profile that predicted the correct power. First, the velocity distribution was simplified to a triangular profile (shown dashed in Fig. 12b). This profile was then systematically adjusted to change the size of the stick and slip areas, while continuing to capture the essential physics of the contact. Fig. 14 illustrates the calibration procedure. In the central sticking zone, the velocity increases linearly with radius, and is equal to the nominal tool velocity. It then falls linearly to zero at the boundary of the slip zone. The outer radius of the slip zone was initially equal to the tool radius, R_o = 5 mm, with the peak velocity located at 0.6 R_o (as a simple fit to the profile inferred from the marker experiments, Fig. 12b). In the reverse-engineered analysis, the velocity profile was re-scaled empirically for each run of the deformation model to match the instantaneous power measured experimentally. A simple one-parameter method of scaling was used, as shown in Fig. 14: the outer radius R′ was reduced, while maintaining the boundary between the stick and slip zones at 0.6 R′.

The results of this calibration of the deformation model are presented in Fig. 15. A close match of the power history was readily achieved for all materials, and for both rotational speeds, as shown by the datapoints for predicted power, compared to the continuous experimental curves. The figures also display the outer radius of the slip zone, R′, which was the calibration parameter. As expected, the effective radius R′ is always smaller than the tool radius (R_o = 5 mm), but

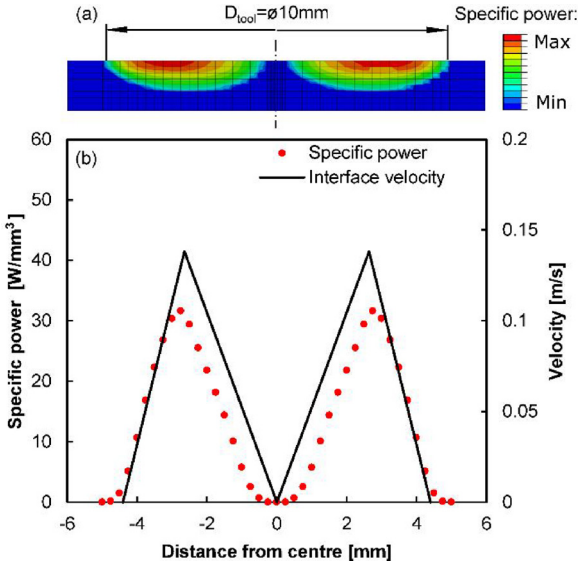

Fig. 16. (a) FE map of heat generated across a weld cross-section in a typical snapshot of the deformation; (b) resultant radial distribution of specific power, averaged through-thickness [LH axis], and the inferred velocity profile, specified as a boundary condition in the deformation model [RH axis]. Sample weld in Al 6082-T6 at 500 rpm, snapshot after 1.6 s.

reduces steadily with time, thereby reducing the deformation zone size, the maximum velocity, and the resultant heat generation.

At 500 rpm, the adjusted radius R′ falls from a peak value around 80–90% of the shoulder radius R_o to around 60–70% R_o. At 2000 rpm, the calibrated radius peaks around 60–80% of R_o and decays to 40–50% R_o. These changes in contact conditions are physically conceivable, bearing in mind the softening of the material and the falling downforce. It may also be noted that, in a CFD-based model of FSW, Colegrove et al. (2007) found that the weld power could only match measured temperature data by reducing the contact radius to 80% of the tool radius. It is therefore concluded that the velocity profile under the tool does evolve throughout welding, and that a lower effective contact radius is the principle reason for the heat generation being lower than expected at higher rotation speeds. Other variants of the velocity profile with time may of course apply, and it may be possible to infer more detail from further marker experiments. In some micrographs in Reilly et al. (2015)), the edge of the layered zone does indeed appear at a smaller radius than the shoulder, but as the weld time increases the number of layers becomes too high to resolve accurately.

Fig. 16 shows the distribution of heat generation predicted by the deformation model, superimposed on the velocity profile at a given instant. The predicted power does not rise quickly with radius from the centre, due to the contribution of the initial elastic loading in the small-strain model, shown in Fig. 2d. To reduce this effect, the rotation in each snapshot could be increased above 1°. But the error is small, and larger rotations increase mesh distortion and computation time. Overall, the shape of the profiles shows the close correlation between interface conditions and heat generation, and justifies the simplified triangular profile of heat generation assumed in the thermal model. However, determining the locations of the two characteristic points – the peak, and the outer contact radius – and how these evolve with dwell time, requires further experimental investigation of material flow.

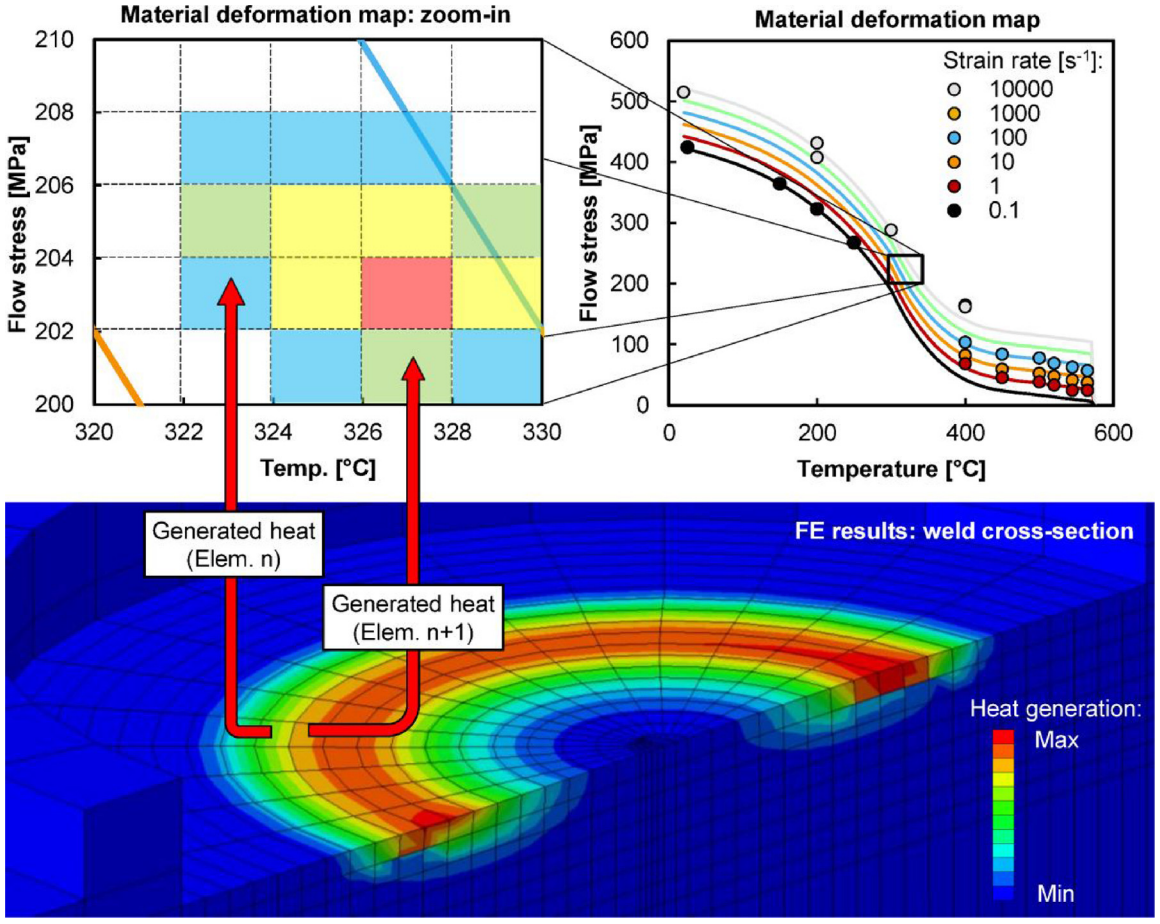

Fig. 17. Mapping heat generation onto constitutive data in a material deformation map.

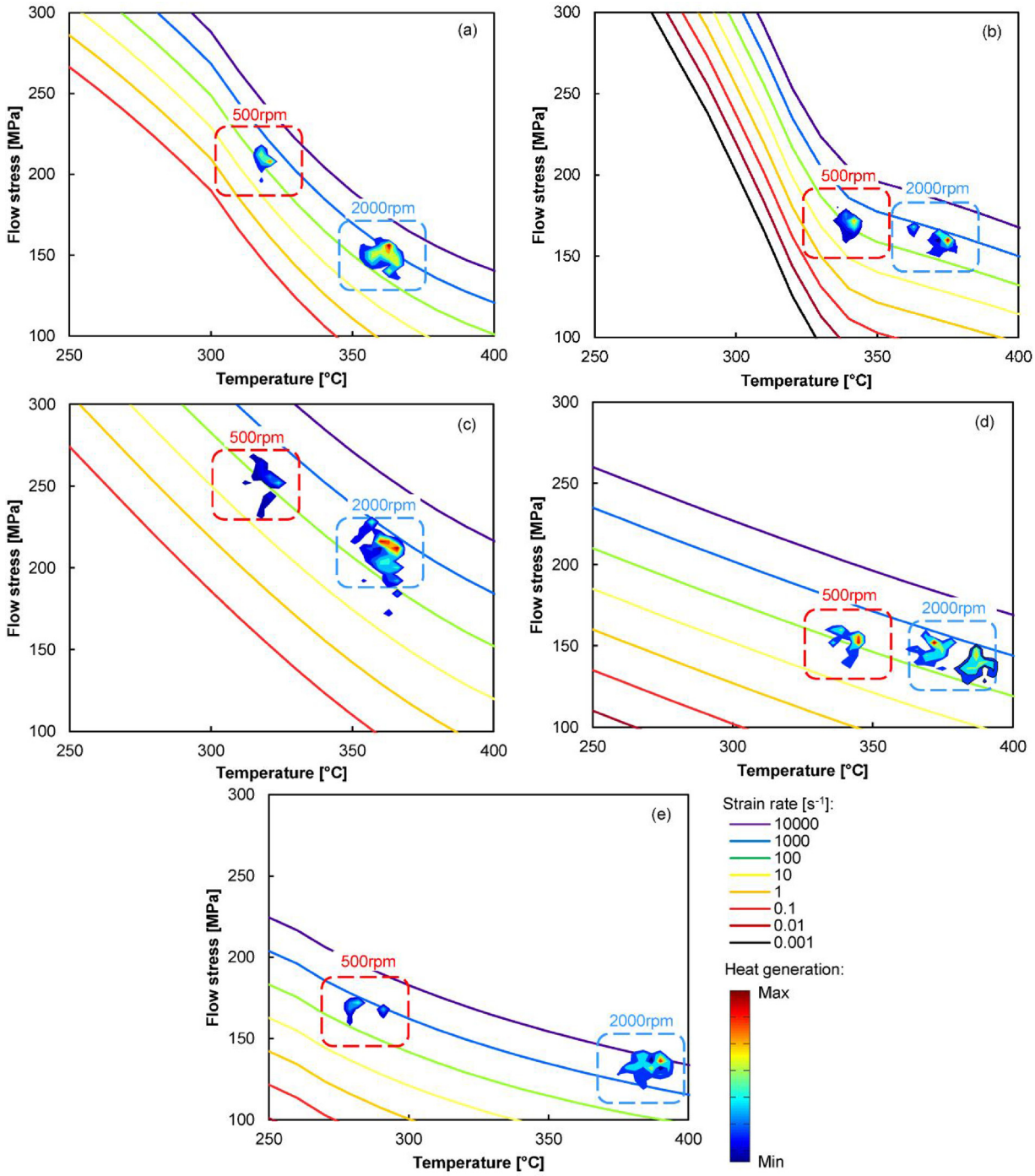

Fig. 18. Material deformation maps for welds at 500 rpm and 2000 rpm: (a) Al 6082; (b) Al 2024; (c) Al 7449; (d) AlSi10Mg; (e) Mg AM50. The sub-region of the full constitutive data shown is indicated in Fig. 10.

5.1. Material deformation maps

An approach to visualisation of the material deformation behaviour during welding, in relation to the constitutive response, was proposed by Colegrove and Shercliff (2006) and Colegrove et al. (2007) in their CFD modelling of FSW in various aluminium alloys. The method is to overlay contours on the constitutive data plot showing the probability that material will experience the given deformation conditions. These 'material deformation maps' highlight the dominant temperature and strain-rate regime for the plastic regions in FS welds. This approach helps to understand the limiting effect of material softening behaviour, and may provide a practical tool for selection of parameter windows or alloys with a desirable constitutive behaviour.

The present work modifies Colegrove et al.'s approach, displaying the share of the total *amount of heat* generated in a given set of deformation conditions, rather than the probability that they will occur. As conditions are tested increment-by-increment and element-by-element, the heat generated in each volume may be associated with a given set of material conditions for that volume (Fig. 17). Consider a model with a total number of elements, I. At its centroid, an element i has a temperature T_i and von Mises stress σ_i, while the rate of plastic dissipation within the element is equal to P_i. The total amount of heat generated under given conditions is mapped by discretising the temperature and von Mises stress into small intervals, i.e. between

temperatures T_M and $T_M + \Delta T$, and von Mises stresses σ_N and $\sigma_N + \Delta\sigma$. The procedure is repeated for each increment j in the total number of increments, J, in a given small-strain simulation, and for each small-strain simulation k in the total number of simulations, K. The time increment between a small strain simulation k and $k+1$ is equal to Δt_k. The discretised heat input can then be expressed as:

$$Q_{M,N} = \sum_{k=1}^{K}\sum_{j=1}^{J}\sum_{i=1}^{I}\begin{cases} T_i \in (T_M,\ T_M + \Delta T) \wedge \sigma_i \in (\sigma_N,\ \sigma_N + \Delta\sigma) & P_{i,j,k}\Delta t_k \\ else & 0 \end{cases}$$

Given a sufficiently fine mesh size, as well as constant, small increments of temperature ΔT and stress $\Delta\sigma$, a continuous distribution of heat generation $Q_{M,N}$in terms of T_M and σ_N can be plotted as a contour map, superimposed on the constitutive data curves (Fig. 17).

Fig. 18 shows material deformation maps for the autogenous FSSW welds for all five alloys, for both 500 and 2000 rpm. All the maps refer to predictions of the small-strain model with the slip zone radius varying with time. The results show that, for each rotation speed, the deformation conditions are consistently localised to a characteristic domain. The majority of heat generation takes place in a strain-rate regime between 100 and 1000 [1/s], and a temperature regime between 300 °C and 400 °C. These strain-rate and temperature regimes correspond to the period when conditions effectively reach a steady-state, for welds of 30 s duration. As expected, the temperatures at 2000 rpm are on average 50 °C higher than those at 500 rpm, and at higher strain-rate and lower flow stress. The effect of rotation speed varies from alloy to alloy, so it remains unclear why the resulting power histories coincide in each alloy, when the speed was increased by a factor of 4. But the analysis illustrates how the self-stabilising effects of material softening and heat generation, common to all friction processing, tend towards a “sweet spot” in deformation conditions where thermomechanical balance is achieved.

6. Conclusions

An FE deformation model was developed successfully for friction stir spot welding with the following novel characteristics:

- heat generation in a large strain welding process was predicted using small-strain “snapshot” models run at intervals, with the temperature field imported from a continuous thermal model (avoiding computationally expensive remeshing and solution methods);
- the tool-workpiece contact conditions were specified kinematically as a radial variation in circumferential velocity, with inner stick and outer slip zones, as inferred from marker experiments and analytical modelling (avoiding arbitrary assumptions about friction conditions);
- heat generation was predicted directly from the hot constitutive responses of the workpiece alloys, using curve-fits to collated data (avoiding the common assumption of validity of Johnson-Cook models).

The model predictions were validated against two independent measurements of power history (from torque data, and thermal modelling of thermocouple data). Five diverse Al and Mg alloys were studied at two rotation speeds, using a custom-designed FSSW rig. The key observations were as follows:

- the measured power histories were remarkably similar across all five alloys and both rotation speeds;
- the model indicated that this behaviour was consistent with the evolution of the effective contact radius between tool and workpiece during welding;
- novel ‘material deformation maps’ revealed that, for a given weld, the hot deformation conditions converge to a narrow window of temperature and strain-rate, maintaining the balance between material softening and heat generation.

Acknowledgements

The work described in this paper was initially funded by the UK Engineering and Physical Sciences Research Council (EPSRC) via the grant Friction Joining – Low Energy Manufacturing for Hybrid Structures in Fuel Efficient Transport Applications (EP/G022674/1), and subsequently by EPSRC through the University of Cambridge Doctoral Training Account, with additional CASE award funding from TWI. The authors gratefully acknowledge the technical discussions with: Graham McShane and Aidan Reilly (University of Cambridge); Philip Prangnell, Joe Robson and Yingchun Chen (University of Manchester); and Mike Russell, Kathryn Beamish and Chris Stanhope (TWI). We also thank Paul Clark, Naveed Iqbal and Levi Rotherham (TWI), and Simon Marshall (UC) for their assistance with the experiments.

References

Awang, M., Mucino, V., 2010. Energy generation during friction stir spot welding (FSSW) of Al 6061-T6 plates. Mater. Manuf. Processes 25 (1-3), 167–174.
Badarinarayan, H., Hunt, F., Okamoto, K., 2007. Friction stir spot welding. Friction Stir Welding and Processing. ASM International, Materials Park, Ohio, pp. 235–272.
Bae, D.H., Lee, M.H., Kim, K.T., Kim, W.T., Kim, D.H., 2002. Application of quasicrystalline particles as a strengthening phase in Mg–Zn–Y alloys. J. Alloys Compd. Compd.342 (1-2), 445–450.
Bakavos, D., Prangnell, P.B., 2009. Effect of reduced or zero pin length and anvil insulation on friction stir spot welding thin gauge 6111 automotive sheet. Sci. Technol. Weld. Join. 14 (5), 443–456.
Bakavos, D., Chen, Y., Babout, L., Prangnell, P., 2010. Material interactions in a novel pinless tool approach to friction stir spot welding thin aluminum sheet. Metall. Mater. Trans. A 42A, 1266–1282.
Bhimavarapu, S.B., Maheshwari, A.K., Bhargava, D., Narayan, S.P., 2011. Compressive deformation behavior of Al 2024 alloy using 2D and 4D processing maps. J. Mater. Sci. 46 (9), 3191–3199.
Cepeda-Jiménez, C.M., Ruano, O.A., Carsí, M., Carreño, F., 2012. Study of hot deformation of an Al–Cu–Mg alloy using processing maps and microstructural characterization. Mater. Sci. Eng. A 552, 530–539.
Chen, Y.C., Liu, S.F., Bakavos, D., Prangnell, P.B., 2013. The effect of a paint bake treatment on joint performance in friction stir spot welding AA6111-T4 sheet using a pinless tool. Mater. Chem. Phys. 141 (2-3), 768–775.
Chen, L., Zhao, G., Gong, J., Chen, X., Chen, M., 2015. Hot deformation behaviors and processing maps of 2024 aluminum alloy in as-cast and homogenized states. J. Mater. Eng. Perform. 24 (12), 5002–5012.
Chen, G., Ren, C., Ke, Z., Li, J., Yang, X., 2016. Modeling of flow behavior for 7050-T7451 aluminum alloy considering microstructural evolution over a wide range of strain rates. Mech. Mater. 95, 146–157.
Colegrove, P.A., Shercliff, H.R., 2004. Two-dimensional CFD modelling of flow round profiled FSW tooling. Sci. Technol. Weld. Joi. 9 (6), 483–492.
Colegrove, P.A., Shercliff, H.R., 2005. 3-Dimensional CFD modelling of flow round a threaded friction stir welding tool profile. J. Mater. Process. Technol. 169 (2), 320–327.
Colegrove, P.A., Shercliff, H.R., 2006. CFD modelling of friction stir welding of thick plate 7449 aluminium alloy. Sci. Technol. Weld. Join. 11 (4), 429–441.
Colegrove, P.A., Shercliff, H.R., Zettler, R., 2007. Model for predicting heat generation and temperature in friction stir welding from the material properties. Sci. Technol. Weld. Join. 12 (4), 284–297.
Corning SAS, 2012. (n.d.). Macor: Machinable Glass Ceramic For Industrial Applications. Retrieved January 2017, 9, from. https://www.corning.com/media/worldwide/csm/documents/71759a443535431395eb34ebead091cb.pdf.
Dickerson, T., Shi, Q., Shercliff, H.R., 2003. Heat flow into friction stir welding tools. 4th International Symphosium on Friction Sitr Welding.
Ding, H., Hirai, K., Homma, T., Kamado, S., 2010. Numerical simulation for microstructure evolution in AM50 Mg alloy during hot rolling. Comp. Mater. Sci. 47 (4), 919–925.
Estey, C.M., Cockcroft, S.L., Maijer, D.M., Hermesmann, C., 2004. Constitutive behaviour of A356 during the quenching operation. Mater. Sci. Eng. A 383 (2), 245–251.
Frigaard, O., Grong, O., Midling, O.T., 2001. A process model for friction stir welding of age hardening aluminum alloys. Metall. Mater. Trans. A 32 (5), 1189–1200.
Gerlich, A., Avramovic-Cingara, G., North, T.H., 2006. Stir zone microstructure and strain rate during Al 7075-T6. Metall. Mater. Trans. A 37A, 2773–2786.
Grujicic, M., Pandurangan, B., Yen, C.F., Cheeseman, B.A., 2012. Modifications in the AA5083 Johnson-Cook material model for use in friction stir welding computational analyses. J. Mater. Eng. Perform. 21 (11), 2207–2217.
Gupta, S., Abotula, S., Shukla, A., 2014. Determination of Johnson–Cook parameters for cast aluminum alloys. J. Eng. Mater. Technol. 136 (3), 034502 1-4.

Hirasawa, S., Badarinarayan, H., Okamoto, K., Tomimura, T., Kawanami, T., 2010. Analysis of effect of tool geometry on plastic flow during friction stir spot welding using particle method. J. Mater. Process. Technol. 210 (11), 1455–1463.
Jaspers, S.P.F.C., 1999. Metal Cutting Mechanics and Material Behaviour. PhD thesis. Eindhoven, The Netherlands: Technische Universiteit, Eindhoven.
Jedrasiak, P., 2012. Modelling of Friction Stir Spot Welding (MPhil thesis). Cambridge University Engineering Department, Cambridge, UK.
Jedrasiak, P., 2017. Thermomechanical Modelling of Friction Welding. PhD thesis. Cambridge University Engineering Department, Cambridge, UK.
Jedrasiak, P., Shercliff, H.R., 2017. An Instrumented Rig for Alloy Characterisation in Autogenous Friction Stir Spot Welding (2017). Cambridge University Engineering Department Technical Report, Cambridge, UK CUED/C-MATS/TR263, March 2017.
Jedrasiak, P., Shercliff, H.R., Reilly, A., McShane, G.J., Chen, Y.C., Wang, L., Robson, J., Prangnell, P., 2016. Thermal modeling of Al-Al and Al-Steel friction stir spot welding. J. Mater. Eng. Perform. 25 (9), 4089–4098.
Johnson, G.R., Cook, W.H., 1983. A constitutive model and data for metals subjected to large strains, high strain rate, and temperatures. 19-21 April. Proceedings 7th International Symposium on Ballistics 541–547.
Karthikeyan, B., Ramanathan, S., Ramakrishnan, V., 2010. A calorimetric study of 7075 Al/SiC composites. Mater. Des. 31, S92–S95.
Kaschnitz, E., Funk, W., Pabel, T., 2014. Electrical resistivity measured by millisecond pulse-heating in comparison to thermal conductivity of the aluminium alloy Al-7Si-0.3Mg at elevated temperature. High Temp. High Press. 43, 175–191.
Khan, A.S., Liu, H., 2012. Variable strain rate sensitivity in an aluminum alloy: response and constitutive modeling. Int. J. Plast. 36, 1–14.
Khosa, S.U., Weinberger, T., Enzinger, N., 2010. Thermo-mechanical investigations during friction stir spot welding (FSSW) of AA6082-T6. Weld. World 54 (5/6), R134–R146.
Kim, D., Badarinarayan, H., Ryu, I., Kim, J.H., Kim, C., Okamoto, K., Wagoner, R.H., Chung, K., 2010. Numerical simulation of friction stir spot welding process for aluminum alloys. Met. Mater. Int. 16 (2), 323–332.
Kumar, A., Mukhopadhyay, A.K., Prasad, K.S., 2009. Superplastic behavior of a high-strength Al-Zn-Mg-Cu-Zr alloy. Metall. Mater. Trans. A 40 (2), 278–281.
Lacki, P., Kucharczyk, Z., Śliwa, R.E., Gałaczyński, T., 2013. Effect of tool shape on temperature field in friction stir spot welding. Arch. Metall. Mater. 58 (2), 595–599.
Lesuer, F., 1999. Experimental Investigations of Material Models for Ti-6Al-4V Titanium and 2024-T3 Aluminum. Lawrence Livermore National Laboratory, Livermore, USA.
Lin, Y.C., Liu, J.J., Chen, J.N., 2013. Material flow tracking for various tool geometries during the friction stir spot welding process. J. Mater. Eng. Perform. 22 (12), 3674–3683.
Lingyun, W., Guangjie, H., Yonge, F., Zhiwen, L., Fusheng, P., 2006. Hot deformation kinetics of magnesium alloy AZ31. J. Wuhan Univ. Technol. Mat. Sci. Edit. 21 (3), 15–17.
Malakizadi, A., Cedergren, S., Sadika, I., Nyborg, L., 2016. Inverse identification of flow stress in metal cutting process using Response Surface Methodology. Simul. Model. Pract. Theory 60, 40–53.
Mishra, R.S., Ma, Z.Y., 2005. Friction stir welding and processing. Mater. Sci. Eng. R Rep. 50 (1-2), 1–78.
Mylonas, G.I., Labeas, G.N., 2014. Mechanical characterisation of aluminium alloy 7449-T7651 at high strain rates and elevated temperatures using split Hopkinson bar testing. Exp. Tech. 38 (2), 26–34.
Nagaumi, H., Suzuki, S., Okane, T., Umeda, T., 2008. Hot tearing of machinability improved 2xxx aluminum alloy of high tin content with manganese and chromium addition. Mater. Trans. 49, 324–330.
Nandan, R., DebRoy, T., Bhadeshia, H.K.D.H., 2008. Recent advances in friction-stir welding - process, weldment structure and properties. Prog. Mater. Sci. 53 (6), 980–1023.
Neto, D.M., Neto, P., 2013. Numerical modeling of friction stir welding process: a literature review. Int. J. Adv. Manuf. Technol. 65, 115–126.
Peel, M.J., Steuwer, A., Withers, P.J., Dickerson, T., Shi, Q., Shercliff, H.R., 2006. Dissimilar friction stir welds in AA5083-AA6082. Part I: process parameter effects on thermal history and weld properties. Metall. Mater. Trans. A 37 (7), 2183–2193.
Reilly, A., 2013. Modelling of Friction Stir Spot Welding. PhD thesis. Department of Engineering, University of Cambridge, Cambridge.
Reilly, A., Shercliff, H.R., McShane, G.J., Chen, Y.C., Prangnell, P.B., 2013. Novel approaches to modelling metal flow in friction stir spot welding. Mathematical Modelling of Weld Phenomena 10. Verlag der Technischen Universität Graz, Austria.
Reilly, A., Shercliff, H.R., Chen, Y., Prangnell, P.B., 2015. Modelling and visualisation of material flow in friction stir spot welding. J. Mater. Process. Technol. 225, 473–484.
Rodríguez-Martínez, J.A., Rusinek, A., Arias, A., 2011. Thermo-viscoplastic behaviour of 2024-T3 aluminium sheets subjected to low velocity perforation at different temperatures. Thin Wall. Struct. 49 (7), 819–832.
Roy, M.J., Maijer, D.M., Dancoine, L., 2012. Constitutive behavior of as-cast A356. Mater. Sci. Eng. A 548, 195–205.
Rudajevová, A., Staněk, M., Lukáč, P., 2003. Determination of thermal diffusivity and thermal conductivity of Mg–Al alloys. Mater. Sci. Eng. A 341 (1-2), 152–157.
Sanjari, M., Farzadfar, S.A., Jung, I.H., Essadiqi, E., Yue, S., 2012. Influence of strain rate on hot deformation behaviour and texture evolution of AZ31B. Mater. Sci. Technol. 28 (4), 437–447.
Schmidt, H., Hattel, J., 2005. A local model for the thermomechanical conditions in friction stir welding. Model. Simul. Mater. Sci. Eng. 13, 77–93.
Schmidt, H., Hattel, J., Wert, J., 2004. An analytical model for the heat generation in friction stir welding. Model. Simul. Mater. Sci. Eng. 12, 143–157.
Seidt, J.D., Gilat, A., 2013. Plastic deformation of 2024-T351 aluminum plate over a wide range of loading conditions. Int. J. Solids Struct. 50 (10), 1781–1790.
Shabgard, M., Seydi, S., Seyedzavvar, M., 2016. Novel approach towards finite element analysis of residual stresses in electrical discharge machining process. Int. J. Adv. Manuf. Tech. 82, 1805–1814.
Slooff, F.A., Dzwonczyk, J.S., Zhou, J., Duszczyk, J., Katgerman, L., 2010. Hot workability analysis of extruded AZ magnesium alloys with processing maps. Mater. Sci. Eng. A 527 (3), 735–744.
Somekawa, H., Hirai, K., Watanabe, H., Takigawa, Y., Higashi, K., 2005. Dislocation creep behavior in Mg–Al–Zn alloys. Mater. Sci. Eng. A 407 (1-2), 53–61.
Song, M., Kovacevic, R., 2003. Thermal modeling of friction stir welding in a moving coordinate system and its validation. Int. J. Mach. Tool. Manu. 43 (6), 605–615.
Song, W.Q., Beggs, P., Easton, M., 2009. Compressive strain-rate sensitivity of magnesium–aluminum die casting alloys. Mater. Des. 30 (3), 642–648.
Su, P., Gerlich, A., North, T.H., Bendzsak, G.J., 2006. Material flow during friction stir spot welding. Sci. Technol. Weld. Join. 11 (1), 61–71.
Takuda, H., Morishita, T., Kinoshita, T., Shirakawa, N., 2005. Modelling of formula for flow stress of a magnesium alloy AZ31 sheet at elevated temperatures. J. Mater. Process. Technol. 164–165, 1258–1262.
Tello, K.E., Gerlich, A.P., Mendez, P.F., 2010. Constants for hot deformation constitutive models for recent experimental data. Sci. Technol. Weld. Join. 15 (3), 260–266.
Threadgill, P.L., Leonard, A.J., Shercliff, H.R., Withers, P.J., 2009. Friction stir welding of aluminium alloys. Int. Mater. Rev. 54 (2), 49–93.
Uematsu, Y., Tokaji, K., Tozaki, Y., Kurita, T., Murata, S., 2008. Effect of Re-filling probe hole on tensile failure and fatigue behaviour of friction stir spot welded joints in Al–Mg–Si alloy. Int. J. Fatigue 30 (10-11), 1956–1966.
Ulysse, P., 2002. Three-dimensional modeling of the friction stir-welding process. Int. J. Mach. Tool. Manu. 42 (14), 1549–1557.
Wang, Y., Jiang, Z., 2012. Dynamic compressive behavior of selected aluminum alloy at low temperature. Mater. Sci. Eng. A 553 (15), 176–180.
Wang, H., Colegrove, P., Mayer, H.M., Campbell, L., Robson, R.D., 2010. Material constitutive behaviour and microstructure study on aluminium alloys for friction stir welding. Adv. Mater. Res. 89-91, 615–620.
Xu, S., Deng, X., Reynolds, A.P., Seidel, T.U., 2001. Finite element simulation of material flow in friction stir welding. Sci. Technol. Weld. Joi. 6 (3), 191–193.
Yamamoto, M., Gerlich, A., North, T.H., Shinozaki, K., 2007. Cracking in the stir zones of Mg-alloy friction stir spot welds. J. Mater. Sci. 42 (18), 7657–7666.
Yang, X.W., Fu, T., Li, W.Y., 2014. Friction stir spot welding: a review on joint macro- and microstructure, property, and process modelling. Adv. Mater. Sci. Eng. Int. J. 697170, 1–11.
Zamani, M., Seifeddine, S., Jarfors, A.E.W., 2015. High temperature tensile deformation behavior and failure mechanisms of an Al–Si–Cu–Mg cast alloy — the microstructural scale effect. Mater. Des. 86, 361–370.
Zhao, F., Li, Y.L., Suo, T., Huang, W.D., Liu, J.R., 2010. Compressive deformation behavior of AZ31 magnesium alloy under quasi-static and dynamic loading. Trans. Nonferrous Met. Soc. China 20 (7), 1316–1320.